Journal of Astronomical Telescopes, Instruments, and Systems

AstronomicalTelescopes.SPIEDigitalLibrary.org

Simulation algorithm to model the visible tunable filter for the Daniel K. Inouye Solar Telescope

Matthias Schubert
Thomas Kentischer
Oskar von der Lühe

SPIE.

Matthias Schubert, Thomas Kentischer, Oskar von der Lühe, "Simulation algorithm to model the visible tunable filter for the Daniel K. Inouye Solar Telescope," *J. Astron. Telesc. Instrum. Syst.* **3**(4), 045002 (2017), doi: 10.1117/1.JATIS.3.4.045002.

Simulation algorithm to model the visible tunable filter for the Daniel K. Inouye Solar Telescope

Matthias Schubert,* Thomas Kentischer, and Oskar von der Lühe
Kiepenheuer-Institut für Sonnenphysik, Freiburg, Germany

Abstract. The visible tunable filter is an imaging spectropolarimeter for solar observations in visible light. The instrument consists of several Fabry–Pérot interferometers (FPIs), a polarization modulator, and a prefilter. It will be one of the first light instruments for the Daniel K. Inouye Solar Telescope (DKIST) on Haleakaláa, Maui, Hawaii. We have developed simulation algorithms to describe the instrument and its impact on scientific observations. Our aim is to study the expected measurement accuracy and to test calibration algorithms. A well-known problem is the surface quality of the glass plates for each FPI. We developed algorithms to describe the influence of a surface microroughness, reflectivity, and figure errors of the individual FPI plates, and the expected total photon flux for scientific data acquisition. This tool is used to derive the limits for manufacturing processes to achieve the measurement accuracy required for science observations with DKIST. [DOI: 10.1117/1.JATIS.3.4.045002]

Keywords: Fabry–Pérot filtergraph; etalon; spectropolarimetry; photon noise; microroughness; Daniel K. Inouye Solar Telescope/visible tunable filter.

Paper 17014 received Apr. 13, 2017; accepted for publication Oct. 3, 2017; published online Nov. 2, 2017.

1 Introduction

The 4-m aperture Daniel K. Inouye Solar Telescope (DKIST), currently under construction on the top of Mt. Haleakalaa on the Hawaiian island of Maui, USA, will be the most powerful solar telescope from the coming decade onward, and the biggest advancement for ground-based solar observations in the near future.[1] DKIST will be capable of observing highly dynamic features with spatial scales of some 20 km in different heights in the solar atmosphere, reaching from the deepest observable photosphere through the chromosphere in the solar corona. The large aperture implies increased spatial resolution and higher sensitivity, ideally suited to study very small concentrations of magnetic fields and their evolution by observing magnetically sensitive absorption lines with high time resolution. Detailed analysis of the spectral distribution of polarization in these lines (which is caused by the Zeeman effect) provides information about the stratification of temperature and velocity fields and the magnetic field vector associated with these structures. They are believed to play a crucial role for the generation, evolution, and dissipation of the highly variable solar magnetic field at larger scales, which constitutes solar magnetic activity and impacts the near-Earth space environment. The construction of DKIST started in 2013 and scientific observations will start in 2020.

The visible tunable filter (VTF) is one of the five first light instruments for the DKIST[2] and is being developed by the Kiepenheuer-Institut für Sonnenphysik (KIS), Freiburg, Germany. VTF is an imaging spectropolarimeter designed for the spectral regime from 520 to 870 nm. The instrument combines two Fabry–Pérot interferometers (FPIs) with slightly different air gaps as the principal devices that provide the required spectral resolution, with an order-selecting interference filter and a polarization modulator. Piezo drives control the width of the air gaps of the FPIs and permit precise tuning of the wavelengths of suitable transmission orders to coincide within the passband of the interference filter. The instrument delivers a two-dimensionally resolved image of the Sun in a narrow spectral band, which can be tuned to scan a solar absorption line, to large format detector arrays that record the polarized intensity at each scan position. Changing the order-sorting interference filter makes other absorption lines within the spectral coverage of the instrument accessible for observations.

The etendue of the FPIs must match the etendue of the telescope for a field of view FOV $= 60$ arc sec to permit observations at the diffraction limit. This requirement results in a clear aperture of an air gap FPI of $D_A = 250$ mm. So far, the largest commercially available FPIs have diameters of $D_A \leq 170$ mm. KIS has therefore established an industrial consortium to build the optics and control elements for FPIs of this size.

In principle, an FPI consists of two partly reflecting glass plates with an air gap in between. The spectral bandwidths are determined by the width of the air gap and the surface reflectivity of the glass plates. Small variations of the gap width result in a shift of the passbands, which in turn produce shifts of the measured line core positions. A gap error of the order of a nanometer will introduce a line shift of a picometer, which translates to errors of several hundred meters per second in inferred Doppler velocities.

Similarly, a reflectivity variation influences the inferred full-width at half-maximum (FWHM) of observed solar line profiles. This can be directly interpreted as an error in derived astrophysical parameters, such as temperature, microturbulence, or the estimated gas pressure. Because we are using two FPIs for the instrument whose errors superimpose randomly, the overall transmission is affected by a spatially varying mismatch between the individual transmission profiles of the interferometers.

*Address all correspondence to: Matthias Schubert, E-mail: schubert@leibniz-kis.de

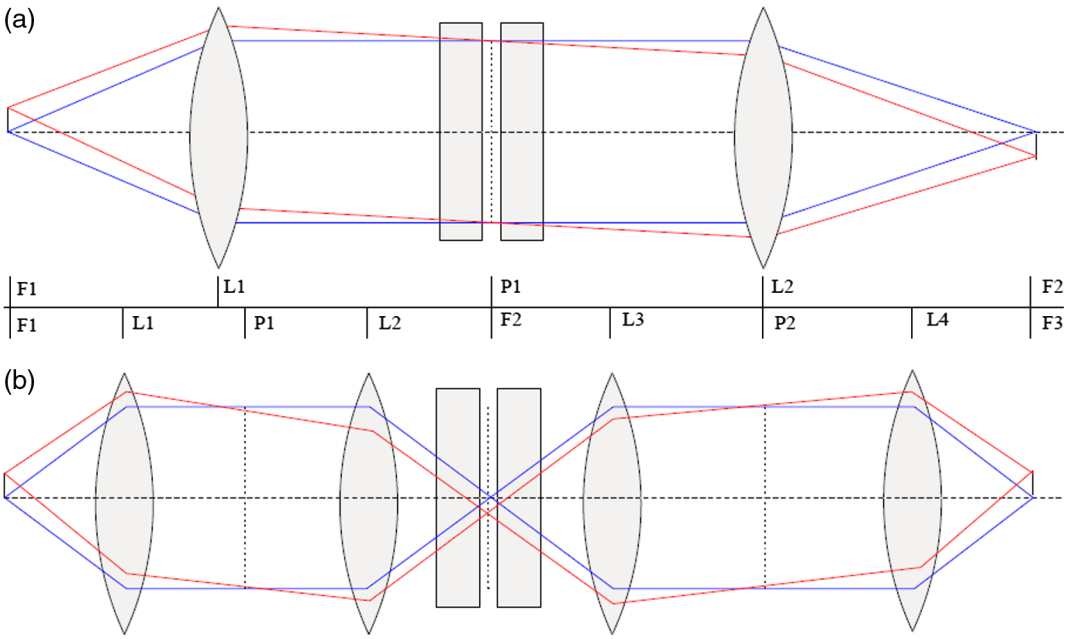

Fig. 1 (a) Collimated mounting of two FPIs and (b) telecentric mounting. The optical setups are drafted with corresponding lenses *L*, focal *F*, and pupil planes *P*.

The challenge is to fulfill the scientific requirements on measurement accuracy for VTF. The requirement for Doppler velocities is 100 m/s, which corresponds to a spectral line shift of $\Delta\lambda = 0.2$ pm at a wavelength of $\lambda = 630.25$ nm. The requirement for magnetic sensitivity translates into a requirement on photometric precision. To achieve a magnetic sensitivity of $B = 20$ G for field lines along the line of sight, the required photometric precision is $\Delta I/I_{\text{cont}} = 2 \cdot 10^{-3}$ at $\lambda = 630.25$ nm.

Obtaining high spatial and spectral-resolved spectropolarimetric data requires an extremely accurate understanding of the instrument and its error contribution on solar observations.

To match the planned measurement accuracy, it was necessary to prestudy errors, which the instrument introduces into scientific observations. Therefore, we developed a simulation algorithm to model solar observations with the DKIST/VTF.

2 Instrument Model

2.1 *Filter Graph*

In the solar community, it is common to use FPIs in imaging spectrometers to obtain highly spatial and spectral-resolved filter graphs of the solar surface. There are two different mounting possibilities in the optical path, which are shown in Fig. 1 for a single FPI. The collimated setup is shown in the upper part and the telecentric mounting is below. The drafts show the optical setups with lenses and their corresponding focal and pupil planes. The VTF is designed for telecentric mounting. Well-known instruments in telecentric mounting are, e.g., the CRisp Imaging Spectro Polarimeter and Swedish Solar Telescope (CRISP/SST: see Ref. 3) and the Triple Etalon SOlar Spectrometer at the Vacuum Tower Telescope (VTT) on Tenerife (TESOS/VTT: see Ref. 4). For the collimated mounting, the GREGOR Fabry–Pérot-Interferometer (Ref. 5) and the Interferometric BIdimensional Spectrometer (Ref. 6) are famous instruments.

2.1.1 *Fabry–Pérot interferometer*

In general, an FPI consists of two glass plates with partly reflecting coatings and an adjustable air gap g in between. A detailed description of the theory can be found in Ref. 7 and is briefly described here to mainly understand the principles for the presented simulation algorithm. Figure 2 shows a scheme of the optical path inside the cavity for a single incoming beam S_0. The path difference Δl for beam S_1 and S_2 is colored with turquoise and red. Constructive interference occurs if the path difference Δl is a multiple of the incoming wavelength λ. In the following, equations for quasimonochromatic light will be given to describe the transmission profile of FPIs. For nonmonochromatic light, the resulting intensity for different wavelengths is calculated according to the superposition principle.

$$\Delta l = m \cdot \lambda = 2 \cdot n' \cdot g \cdot \cos(\theta'). \tag{1}$$

The refraction index is denoted by n', the gap between FPI glass plates by g, the spectral order by m, and the angle for the incoming light by θ'. For constructive interference, this leads to the phase term

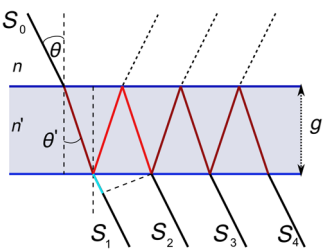

Fig. 2 Optical path for a single beam, which is repeatedly reflected between two partially coated glass plates.

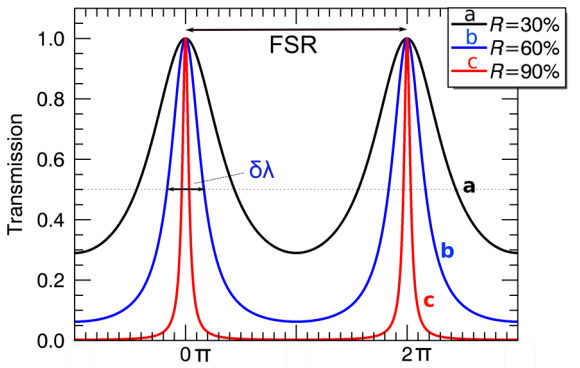

Fig. 3 Transmission profile (FPI) for different reflections R of the coatings.

$$\psi = \frac{4\pi}{\lambda} n' \cdot g \cdot \cos(\theta'). \tag{2}$$

The reflectivity coefficient is expressed by r, r' and the transmission by t, t' for both surfaces. The first approximation is to treat the partially reflecting coating of the glass plates as being identical $r = -r'$ and the transmission $t = t'$. Taking into account not only a single beam and summation of the transmitted amplitudes results in the well-known airy-function to model the intensity transmission $f(\lambda)$ for an FPI (with $r^2 = r'^2 = R$ and $t \cdot t' = T$).

$$f(\lambda) = \frac{T^2}{(1-R)^2 + 4 \cdot R \cdot \sin^2\left(\frac{\psi}{2}\right)}, \tag{3}$$

and furthermore with

$$F = \frac{4 \cdot R}{(1-R)^2}, \tag{4}$$

we get a simplified expression for an FPI transmission

$$f(\lambda) = \frac{T^2}{1 + F \cdot \sin^2\left(\frac{\psi}{2}\right)}. \tag{5}$$

Up to now the coatings of the glass plates were treated as ideal. Therefore, the maximum transmission T has to be adjusted because the coatings will absorb a part of the incoming light

$$T = 1 - \frac{A}{1-R}, \tag{6}$$

with absorbency A. Another helpful quantity to understand the transmission profile of an FPI is the free spectral range (FSR) and the finesse ($\mathcal{F}$) (see Fig. 3)

$$\mathrm{FSR} = \frac{\lambda^2}{2 \cdot n' \cdot g \cdot \cos(\theta')}. \tag{7}$$

These two parameters are linked to each other through the FWHM $\delta\lambda$ of the spectral transmission profile

$$\mathcal{F} = \frac{\mathrm{FSR}}{\delta\lambda}, \tag{8}$$

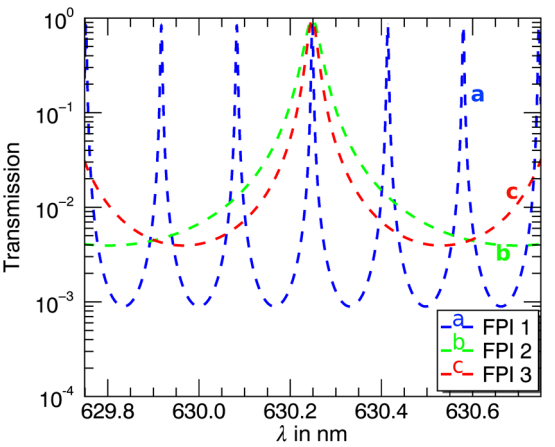

Fig. 4 Transmission profiles for three air gaps g_i.

$$= \frac{\pi}{2}\sqrt{F}. \tag{9}$$

Now, we can give an expression for the FWHM $\delta\lambda$

$$\delta\lambda = \frac{\lambda^2}{2 \cdot n' \cdot g} \frac{1-R}{\pi\sqrt{R}}. \tag{10}$$

In general, these are the quantities to mathematically describe the intensity transmission for one single Fabry–Pérot interferometer. The introduced equations show that the transmission profile is defined by the air gap g, the refraction index n, the angle of incidence θ, and the reflectivity R of the coatings. Figure 3 shows the effect on the profile shape for different reflections R [see Eq. (10)]. Figure 3 also demonstrates that the FSR is independent from the reflectivity R and is mainly adjusted through the air gap g [see Eq. (7)].

2.1.2 *Multiple Fabry–Pérot interferometer in telecentric mounting*

Using FPIs for high-resolution imaging spectrometer demands further steps. The higher/lower spectral passbands have to be suppressed (e.g., see blue transmission profile FPI1 in Fig. 4). Hence, if only one interferometer is used, an observed intensity is contaminated by false light from other spectral regions. To achieve wide spectral scan ranges $\Delta\lambda \gg$ FSR for a high resolving FPI and minimize false light, it is common to use additional FPIs. This is illustrated in Figs. 4 and 5, where FPI1 is the high-resolution FPI. Here, the higher/lower spectral orders are minimized to $\leq 10^{-4}$ for a triple system. Therefore, the simulation algorithm has to model the effect of multiple FPIs on solar observations. The transmission profile $f_{\mathrm{all}}(\lambda)$ for a multi-FPI system is a multiplication of the individual profiles $f_i(\lambda)$ for each FPI

$$f_{\mathrm{all}}(x, y, \lambda) = \prod_{i=1}^{k} f_i(x, y, \lambda). \tag{11}$$

The VTF is designed in a telecentric beam configuration. For imaging a single resolution element, the draft in the bottom of Fig. 1 illustrates the light path for a telecentric mounting on and off the optical axis.

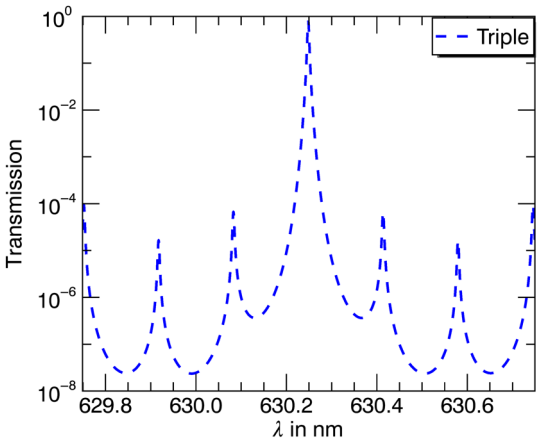

Fig. 5 Combined profile $f(\lambda)$ for three FPIs.

Taking into account surface errors, the light cone for imaging a single resolution element has to be split into separate light rays. Each one sees a different error in the surface quality as Fig. 6 indicates. Therefore, the overall transmission function f_{all} additionally has to be integrated over the angle spectrum of incidence Θ. Because of the telecentric mounting, the angle spectrum $\Theta_{x,y}$ for each resolution element $I'(x,y)$ in the focal plane is identical $\rightarrow \Theta_{x,y} = \Theta$

$$f_{\text{all}}(x,y,\lambda) = \prod_{i=1}^{k} \int_0^{\frac{D_{i,\text{err}}}{2}} \int_0^{2\pi} f_i[x,y,\lambda,\theta(r,\varphi),g(r,\varphi),R(r,\varphi)]\,\mathrm{d}r\,\mathrm{d}\varphi. \tag{12}$$

The coordinates in the focal plane are marked with x and y, and $r_{x,y,i}$ and $\varphi_{x,y,i}$ are the coordinates in the individual FPI plane (see Fig. 7). In Figs. 6 and 7, the green area indicates the relevant region of surface errors that were taken into account to simulate the intensity for one resolution element on the optical axis. The diameter $D_{i,\text{err}}$ of the green area between the FPI plates is defined by the aperture size D_A and the focal length of the imaging system

$$D_{i,\text{err}} = 2 \cdot d_i \cdot \tan\left(\frac{D_A}{2 \cdot f_2}\right), \tag{13}$$

and therefore, the maximum angle of incidence is

$$\theta_{\max} = \arctan\left(\frac{D_A}{2 \cdot f_2}\right). \tag{14}$$

The corresponding wavelength shift $\Delta\lambda_\theta$

$$\Delta\lambda_\theta = \lambda_0[1 - \cos(\theta)], \tag{15}$$

and for a gap error it is calculated as follows:

$$\Delta\lambda_{\text{gap}} = \lambda_0 \frac{\Delta g_i(x,y)}{g}. \tag{16}$$

The overall equation to simulate the detected intensity for each resolution element in the detector plane is given as follows:

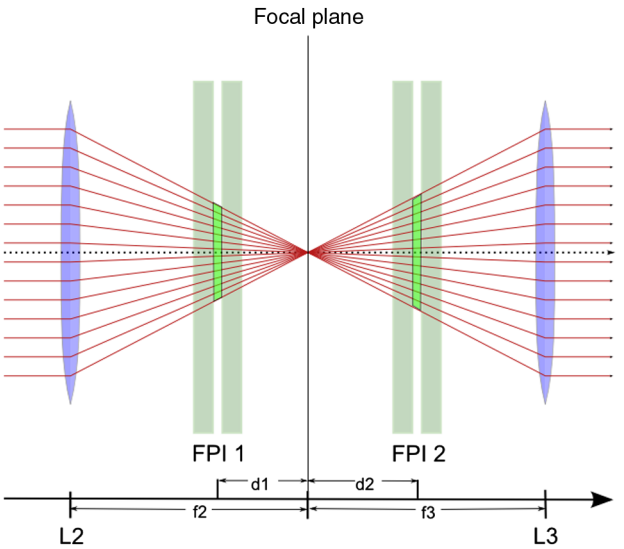

Fig. 6 Ray tracer for two FPIs in telecentric mounting to image a single spot on the optical axis. The distance to the focal plane is $d_{1,2}$. The positions of the lenses are indicated with $L_{2,3}$ and their corresponding focal lengths are $f_{2,3}$.

$$I_{x',y'}(\lambda_{s_t}) = \sum_{\lambda-0.5\text{ nm}}^{\lambda+0.5\text{ nm}} I_{x,y,0}(\lambda) f_{\text{PF}}(\lambda) \prod_{i=1}^{k} \sum_{\Theta} f_{i_{x,y}}[\lambda, \Theta, g_i + t \cdot s_i + \Delta g_{x,y}(\Theta), R_i + \Delta R_{x,y}(\Theta)]. \tag{17}$$

Here, the individual plate errors within the angle spectra are denoted by $\Delta g_{x,y}(\Theta)$ for the gap error and $\Delta R_{x,y}(\Theta)$ for the reflectivity errors. The spectral step width is defined by s_i. This is the change in air gap g_i to shift the transmission maximum by a certain wavelength step $\Delta\lambda$. The number of spectral scan steps is given by $t = \pm 0,1,\ldots,j$ ($2j+1$ is the total number of scan steps). For the simulation algorithm, integration over the angle spectrum Θ and the wavelength λ were numerically approximated with a summation for discrete steps. The amount of plate errors taken into account is defined by the spatial resolution of the surface characterization of the individual FPI plates (see Fig. 6: number of individual rays within the light cone for one resolution element).

2.2 *Polarization Modulator*

Observing the Sun means measuring the intensity. To obtain polarimetric data, an additional filter has to be applied. Stokes developed a formalism to describe partially polarized quasimonochromatic light with four parameters, which is explained in detail in Ref. 7. The effect of optical components (telescope, filters, and polarizer) on intensity measurements can be described with a 4×4-matrix formalism

$$\mathbf{I} = \mathbf{M} \cdot \mathbf{S}, \tag{18}$$

where $\mathbf{I} = (I_0, I_1, I_2, I_3)$ and $\mathbf{S} = (I, Q, U, V)^{\mathrm{T}}$ are the vectors and $\mathbf{M}$ is the overall modulation matrix. The guideline for the modulation scheme was the visible imaging polarimeter at the Observatorio del Teide on Tenerife, which is described in Refs. 8 and 9. Taken ideal optical components into account, a scheme $\mathbf{M}$ can be provided, which modulates the Stokes vector $\mathbf{S}$ to intensities $\mathbf{I}$

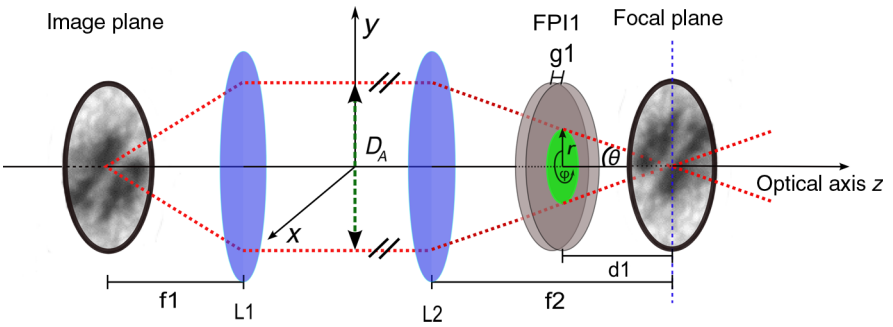

Fig. 7 Amplified draft for FPI1 (see Figs. 1 and 6) to show the coordinate system used in the simulation algorithm.

$$\begin{pmatrix} 1 & \frac{1}{\sqrt{3}} & \frac{1}{\sqrt{3}} & \frac{1}{\sqrt{3}} \\ 1 & \frac{1}{\sqrt{3}} & -\frac{1}{\sqrt{3}} & -\frac{1}{\sqrt{3}} \\ 1 & -\frac{1}{\sqrt{3}} & -\frac{1}{\sqrt{3}} & \frac{1}{\sqrt{3}} \\ 1 & -\frac{1}{\sqrt{3}} & \frac{1}{\sqrt{3}} & -\frac{1}{\sqrt{3}} \end{pmatrix}. \tag{19}$$

The corresponding demodulation matrix $\mathbf{M}'$ with $\mathbf{M}'\mathbf{M} = \mathbf{1}$ to modulate the simulated observed intensities $\mathbf{I}$ to Stokes vectors $\mathbf{S}$ is the following:

$$\begin{pmatrix} \frac{1}{4} & \frac{1}{4} & \frac{1}{4} & \frac{1}{4} \\ \frac{\sqrt{3}}{4} & \frac{\sqrt{3}}{4} & -\frac{\sqrt{3}}{4} & -\frac{\sqrt{3}}{4} \\ \frac{\sqrt{3}}{4} & -\frac{\sqrt{3}}{4} & -\frac{\sqrt{3}}{4} & \frac{\sqrt{3}}{4} \\ \frac{\sqrt{3}}{4} & -\frac{\sqrt{3}}{4} & \frac{\sqrt{3}}{4} & -\frac{\sqrt{3}}{4} \end{pmatrix}. \tag{20}$$

2.3 *Prefilter*

To further suppress the higher/lower spectral orders of an FPI, a prefilter (PF) is used. In principle, a PF consists of a combination of multiple etalons with constant gap g_i between the coatings to define the spectral passband. In the simulation algorithm, the PF transmission f_{PF} is modeled by the following equation:

$$f_{\mathrm{PF}}(\lambda) = \frac{1}{1 + \left[\frac{2\cdot(\lambda-\lambda_0)}{\delta\lambda_{\mathrm{PF}}}\right]^{2n}}. \tag{21}$$

The number of combined etalons (cavities) is indicated with n, λ_0 is the central wavelength of the observed absorption line and $\delta\lambda_{\mathrm{PF}}$ the FWHM. In general, for high-resolution spectropolarimetry, the FWHM of the used PF is in between 0.2 and 1 nm. Filters with $\delta\lambda_{\mathrm{PF}} \leq 0.3$ nm are manufactured with two cavities and have a Gaussian shape, and filters with $\delta\lambda_{\mathrm{PF}} > 0.3$ nm are realized with three and more cavities with a Lorentzian-like overall shape.

3 Error Contribution

We want to study the instrumentally induced errors to define meaningful requirements for the manufacturing process of the etalon plates and mounting on the optical path. Therefore, we have to determine the errors that influence shapes of transmission profiles, the most across the field of view. Studying the solar surface with spectropolarimetric instruments, i.e., measuring magnetic field strengths and Doppler velocities implies that we need very accurately determined line core positions and expected photon flux at the detector plane. As an example for a spectral high-resolution etalon for $\lambda_0 = 630.25$ nm (gap $g = 1.3$ mm, reflectivity $R = 92\%$), errors in line core positions in the range of picometer translate into Doppler velocity error of several hundreds of meters per second. In terms of plate roughness, this corresponds to the gap error of $\approx$1 nm for one etalon [see Eq. (16)]. It is extremely challenging and expensive to get a surface roughness with a standard deviation better than 1 nm with increasing diameter of the etalon plates ($d_{\mathrm{plates_{VTF}}} = 250$ mm). Also, the FWHM is influenced by the plate quality of the etalons [i.e., see Eq. (10)]. This results in a loss of spectral resolution and transmission of the instrument. Therefore, the amount of photons changes in the detector plane. This is crucial for the magnetic sensitivity, i.e., to measure magnetic field strength in line of sight of 20 G it is necessary to have a signal-to-noise ratio SNR $= \frac{N}{\sqrt{N}} \approx 700$ (N is number of photons at detector). Therefore, we modeled the impact of the etalon plate roughness, reflectivity, and the expected photon noise in the presented simulation algorithm. This enables us to put realistic constrains on the plate quality along with the calibration algorithm, which will partly compensate instrumentally induced errors.

3.1 *Photon Flux Budget*

An important factor in modeling the instrument behavior on solar observations is the SNR. The inverse of the SNR defines the relative error contribution on intensity measurement and is Poisson distributed. The magnetic sensitivity is strongly depending on this parameter, because the difference between polarimetric-filtered intensity profiles is evaluated. The SNR is defined as the quotient of total photon number N_{photon} and the root of it

$$\mathrm{SNR} = \frac{N_{\mathrm{photon}}}{\sqrt{N_{\mathrm{photon}}}}. \tag{22}$$

Therefore, a model for the total photon flux budget and thus the observed intensity in the detector plane has to be applied. The total spectral energy flux f_E can be calculated with the Planck function B or taken directly from measurements (see Ref. 10). In the photosphere, f_E can be approximated using the Planck function B for an effective temperature $T_{\mathrm{eff}} \approx 5778$ K.

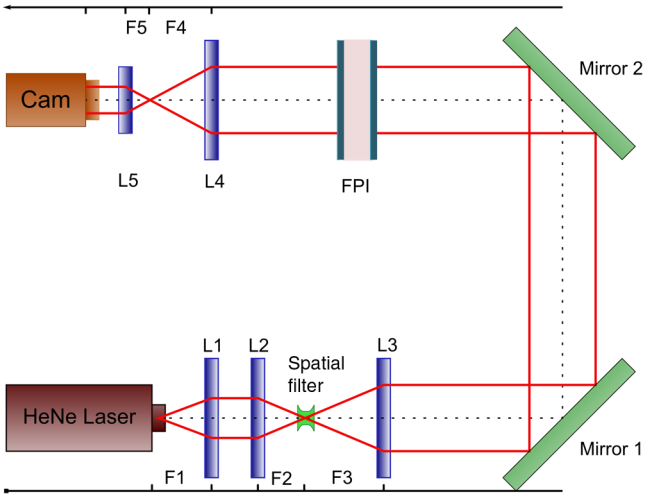

Fig. 8 Experimental setup for the characterization campaign for the surface roughness and reflectivity. Lenses are marked with *L* and the focal lengths with *F*.

$$N_{\text{photon}} \approx \frac{E}{E_{\text{photon}}} = \left[\int_{\lambda_{\min}}^{\lambda_{\max}} B(\lambda, T_{\text{eff}}) \cdot A_{\text{sun}} \cdot \Omega \cdot t_{\text{exp}} \cdot n_{\text{ac}} \cdot e \cdot T_{\text{tel}} \cdot f_{\text{PF}}(\lambda) \cdot f_{\text{all}}(\lambda) \mathrm{d}\lambda\right] / E_{\text{photon}}. \quad (23)$$

The area on the Sun, which is detected in one resolution element, is marked with A_{Sun}, Ω is the solid angle (defined by the telescope diameter and distance to the observed object), e is the quantum efficiency of the detector, t_{exp} is the exposure time, n_{ac} is the number of accumulated detections, and T_{tel} is the overall transmission of the telescope and optical components before the instrument. According to this function, it is possible to approximate the total photon number N_{photon} that is detected and provide a meaningful error on intensity measurements to test, e.g., magnetic sensitivity.

3.2 *Plate Surface Errors—LASER Characterization of a Test System*

To get a realistic spatial distribution of roughness and reflectivity plate errors, a characterization campaign was carried out for the imaging spectropolarimeter at the TESOS/VTT on the Observatorio del Teide on Tenerife (see Refs. 11 and 12). The instrument is designed with three FPIs with a clear aperture of $A_{\text{FPI}} = 50$ mm in telecentric mounting and serves as a test bed for the VTF development. Figure 8 shows the experimental setup for the characterization.

The FPI of interest is illuminated with a HeNe-Laser $\lambda = 632$ nm in a collimated beam configuration. Because of the fact that a monochromatic laser emission profile is approximately a Dirac delta function, it can be used to sample the transmission profile $f_{i_{x,y}}(\lambda)$ for each FPI. With the given formulas above, it can be shown that an error in the gap $\Delta g_i(x, y)$ in between the glass plates is translated into a spectral shift $\Delta\lambda(x, y)$ of the transmission profile $f_{i_{x,y}}(\lambda)$

$$\Delta g(x, y) = \frac{\Delta\lambda(x, y)}{\lambda_0} \cdot g. \quad (24)$$

Also, the reflectivity error distribution can be derived from laser characterizations. The following equations demonstrate the connection between the finesse $\mathcal{F}$ and the FWHM $\delta\lambda$. Therefore, the reflectivity $R_{i_{x,y}}$ is

$$\mathcal{F}(x, y) = \frac{\pi}{2}\sqrt{\frac{4R(x, y)}{[1 - R(x, y)]^2}} = \lambda_0^2/[2ng \cdot \delta\lambda(x, y)], \quad (25)$$

$$C(x, y) = \left[\frac{\lambda_0^2}{\pi n \cdot g\delta\lambda(x, y)}\right]^{-2}, \quad (26)$$

$$R_{1,2}(x, y) = 1 + 2 \cdot C(x, y) \pm \sqrt{4 \cdot C(x, y) + 4 \cdot C(x, y)^2}. \quad (27)$$

Evaluation of the wavelength shifts $\Delta\lambda_{x,y}$ and the FWHM $\delta\lambda_{x,y}$ for each pixel in the detector plane results in a two-dimensional (2-D) map of the gap $\Delta g(x, y)$ and reflectivity errors $\Delta R(x, y)$ for the illuminated region of the characterized FPI. Figure 9 shows measured transmission profiles $f_i(\lambda)$ for each etalon.

Applying a Lorentzian fit to the measured transmission profiles $f_{i,x,y}(\lambda)$ results in a wavelength shift and reflectivity variation across the illuminated area of the characterized FPI. The results for the spatial gap error distribution $\Delta g(x, y)$ are shown in Figs. 10(a) to 10(c) and for the reflectivity error $\Delta R(x, y)$ in Figs. 11(a) to 11(c).

The root mean square (rms) values for the plate gap errors are as follows:

- FPI1: $\Delta g_1 = 1.45 \pm 0.05$ nm
- FPI2: $\Delta g_2 = 1.19 \pm 0.03$ nm
- FPI3: $\Delta g_3 = 1.33 \pm 0.02$ nm.

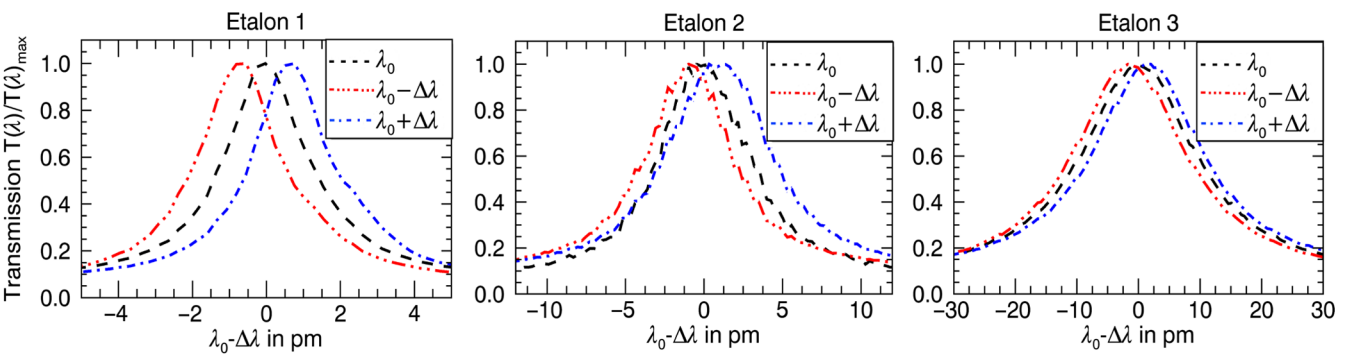

Fig. 9 Measured transmission profiles $f_i(\lambda)$ for different detector elements for each etalon (FPI1 to 3).

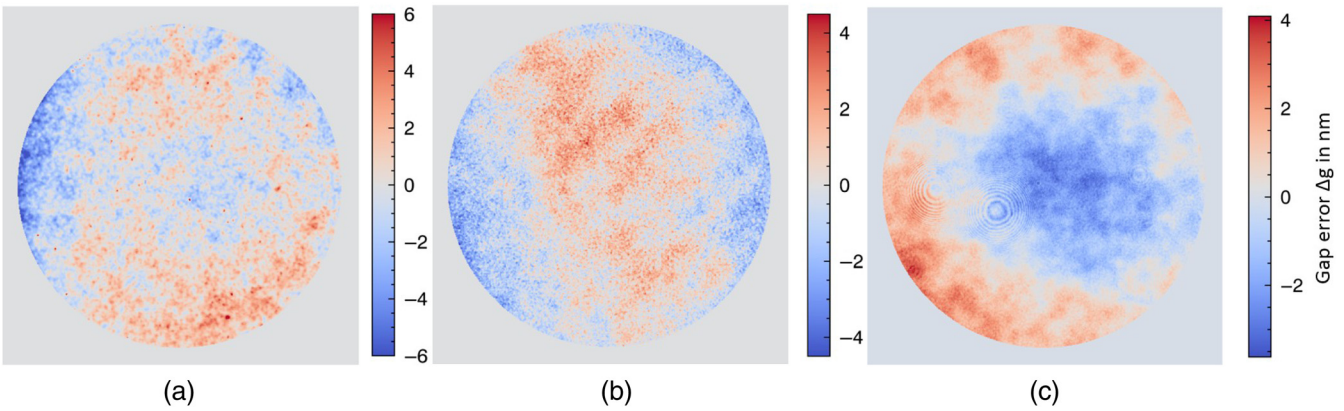

Fig. 10 Calculated 2-D maps of microroughness for the individual FPIs: (a) FPI 1, (b) FPI 2, and (c) FPI 3.

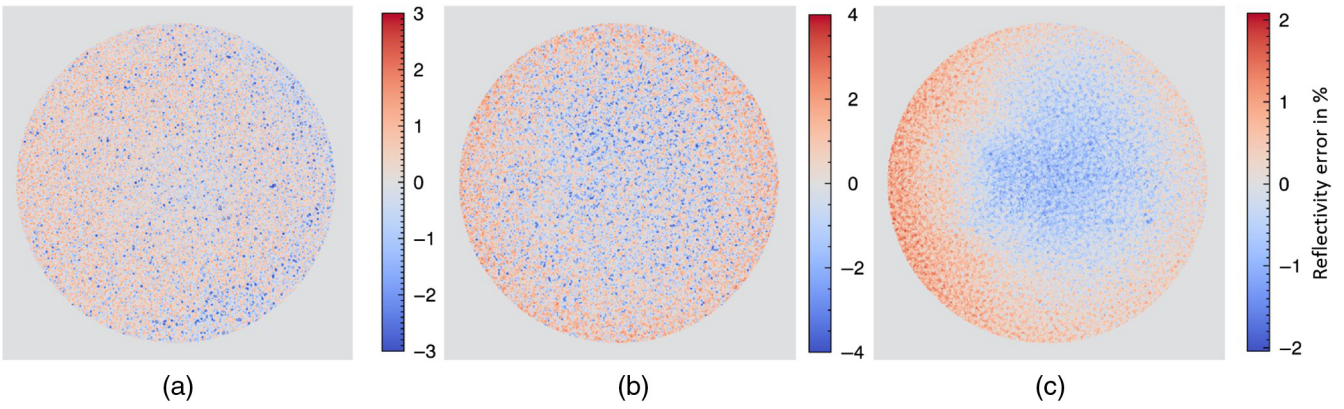

Fig. 11 Calculated 2-D maps of the reflectivity variation $\Delta R(x, y)$ across the FPI: (a) FPI 1, (b) FPI 2, and (c) FPI 3.

The averaged reflectivity was also calculated:

- FPI 1: $R_1 = 93.7 \pm 0.9\%$
- FPI 2: $R_2 = 91.0 \pm 1.2\%$
- FPI 3: $R_3 = 80.2 \pm 0.5\%$.

The reflectivity error distribution $\Delta R(x, y)$ is calculated as the local deviation to the above-given averaged values for each FPI.

Taking a closer look at the results illustrates that the spatial error distributions is a combination of microvariations and big scale figure errors. Therefore, it is meaningful to apply different 2-D error maps in the simulation algorithm to distinguish between the effects on simulated observations for different spatial error distributions. The applied 2-D-error maps of the etalon plate surface quality directly give us the opportunity to test a wide range of combinations for error distributions within the angle spectrum Θ for a resolution element.

4 Results

A multi-Etalon simulation algorithm was developed to model the instrumental impact on scientific observations with the DKIST/VTF. The software is programmed in the interactive data language (IDL) and is available to the solar community. The algorithm is highly customizable to test and compare different instrument configurations. The necessary input parameters are listed in Tables 1–3.

To model the photon noise in solar observations, a pseudorandom number generator was used. The applied algorithm is explained in Ref. 13 and implemented in IDL by the function randomn. According to the calculated detected photons, the relative noise defines the rms value for the random number generator randomn that is additionally applied to the line profiles.

The integration over the angles $\Theta_{x,y}(r, \varphi)$ is implemented explicitly in the algorithm and is not approximated with an angle finesse $\mathcal{F}_\Theta$. Because of microroughness, individual light rays within one light cone for one detection element see different errors in the gap, and therefore the transmission profiles $f_{i,x,y}(\lambda)$ will be spectral shifted additionally by $\Delta\lambda_{\text{gap}}$ [see Eq. (16)]. As a consequence, the effect on transmission profiles $f_{i,x,y}(\lambda)$

Table 1 Instrument parameter.

–Full Stokes data cube $S[I(x, y, \lambda), Q(x, y, \lambda), U(x, y, \lambda), V(x, y, \lambda)]$
–Modulation scheme M
–Number of FPIs (up to three)
–Air gap g_i and reflectivity R_i for each FPI
–f-number $f\# = \frac{f}{D_A}$ (defines Θ_{max})
–Distances d_i of the FPIs to the focal plane

Table 2 Input variables for the simulated observations.

–Central wavelength λ_0
–Scan region
–Scan step size $\Delta\lambda$ (defines s_i)
–Number of scan steps t
–Region of interest

Table 3 Error contribution input.

–2-D maps for the reflectivity $\Delta R(x,y)$ in percent and gap error $\Delta g(x,y)$ in meter
–Telescope diameter D_T and overall transmission T_{tel} before the instrument
–Exposure time t_{exp}
–Number of accumulated observations n_{ac}

Table 4 Parameters to simulate a triple-FPI system with high spectral resolution. Figure 4 illustrates ideal transmission profiles $f(\lambda)$ with the given parameters for each etalon.

FPI	plate separation g	Reflectivity R	spectral order for $\lambda_0 = 630.25$ nm
1	1.2 mm	94%	3808
2	0.222 mm	88%	704
3	0.3516 mm	88%	1116

[respectively on simulated sampled intensity profiles $I_{i,x,y}(\lambda)$] would not be modeled correctly with an approximated angle finesse $\mathcal{F}_\Theta$ only [see for Eq. (15)]. In the presented simulation algorithm, we take care of both effects to model the instrument behavior. Summation of the individual rays results in a spectrally shifted, asymmetric, and broadened overall profile $f_{\text{all},x,y}(\lambda)$ for each detection element, which now can be studied in a meaningful way.

First, we modeled the transmission profiles $f_{\text{all}}(x,y)$ for a triple-FPI configuration (see for Table 4) and compared them to an ideal instrument profile $f_{\text{ideal}}(\lambda)$. Figure 12 shows simulated transmission profiles $f_{\text{all}}(\lambda)$ for random positions in a simulated region of interest of 5×5 arcsec. Here, the measured 2-D error maps [shown in Figs. 10(a), 10(b), and 10(c)] were applied in the simulation, e.g., to study the instrument transparency T.

The corresponding error distributions for each etalon are plotted in Fig. 13 with $\Delta g_{\text{rms}} = 1.5$ nm. The spectral resolution is $\text{SR} = \lambda/\delta\lambda \approx 170{,}000$ at a central wavelength $\lambda_0 = 630.25$ nm.

Because of the mismatch between the transmission functions of the individual FPI, a strong dependence of the instrument throughput on the plate separation errors $\Delta g_i(x,y)$ can be

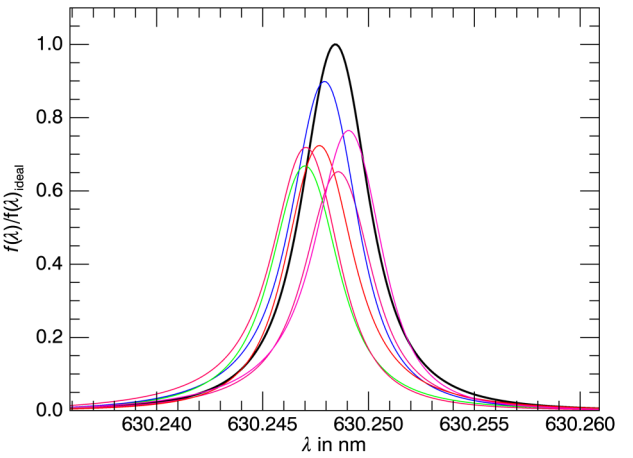

Fig. 12 Comparison of an ideal transmission function $f_{\text{ideal}}(\lambda)$ (black) and $f_{\text{all},x,y}(\lambda)$ (colored), which correspond to the simulated instrument transmission for random points in the field of view.

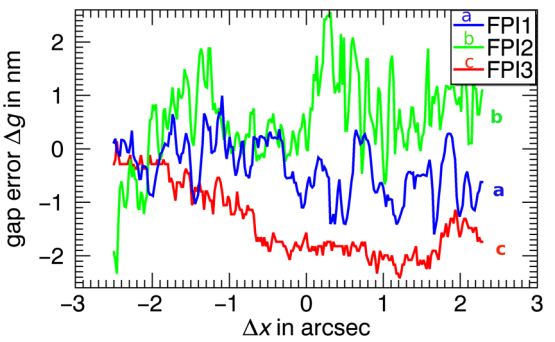

Fig. 13 Slice through the middle of measured 2-D error maps [Figs. 10(a) to 10(c)], which corresponds to the simulated transmission profiles in Fig. 12.

shown. Moving the FPIs away from the focal plane will reduce the loss in photons. Figures 14 and 15 show a slice through simulated transmission profiles for a circular field of view with diameter $D_{\text{FOV}} = 5$ arc sec. These further simulations were performed for different rms gap errors Δg_{rms}. Figure 15 compared to Fig. 14 shows the improvement due to a defocused mounting of the etalons to the focal plane for distances $d_1 = d_2 = |0.5\text{ m}|$ and $d_3 = 0.7$ m. As a result, it could be demonstrated that the dependency on gap variations $\Delta g_i(x,y)$ is reduced, and the overall transparency of the instrument can be improved.

5 Limitations of the Model

We suggest that designing an instrument for spectropolarimetric observations demands a narrow bandwidth in the order of picometer and sufficient photons to study the solar surface in terms of Doppler velocities and magnetic field strength. In the presented simulation algorithm, we assume for an air gap etalon identical reflectivity coefficients for each plate within the cavity, which are frequency independent for a spectral range $\gg$FSR. Reference 14 describes the influence of low- and frequency-dependent reflectivity etalons and evaluates transmission profiles for different scenarios. It introduces a Lorentzian function to describe the losses of a Fabry–Pérot interferometer. In the present model, we put the limits on the reflectivity to $R \geq 60\%$ and neglected the frequency dependence. We also assume that

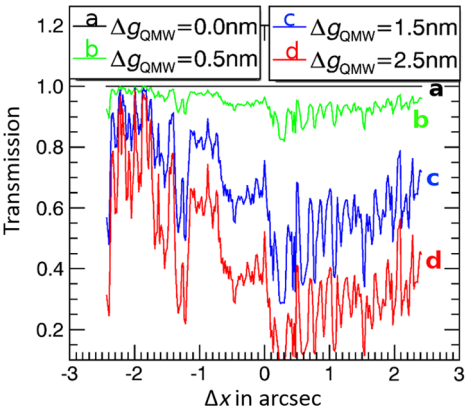

Fig. 14 FPIs theoretical in focal plane.

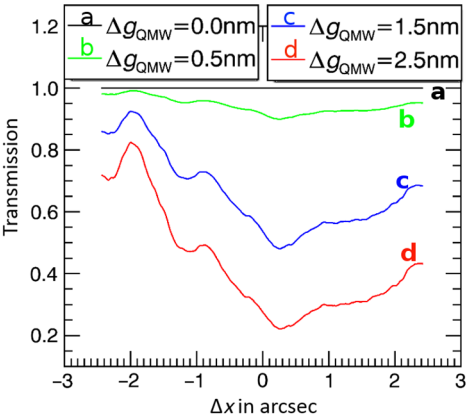

Fig. 15 Defocused mounting of FPIs.

the coatings of the plates have very low absorption in the order of ≈0.2%. Therefore, we describe the individual spectral transmission profiles $f_{x,y}(\varphi)$ and losses using Airy functions, which are integrated over the angle spectrum Θ for each detector element. The main source of the transmission profiles distortion is the plate microroughness (see Fig. 12). The summation of the individually shifted Airy functions across the angle spectrum Θ produces nonuniform shapes and shifts of the instrumental profiles, which defines the expected photon flux in the detector plane.

The effects of ghost images due to reflections between the individual etalons have not been modeled currently. References 12 and 15 explain in detail that tilting the FPIs with the smallest gap g by a small angle will strongly decrease the image distortion by reflections between the etalons. We expect that all etalon plates are slightly wedged. By this, all the ghost reflections between the outer etalon surfaces and the active cavity surfaces can be eliminated at a pupil stop located in the reimaging optical path. Ghost reflections between the individual etalons are eliminated in the same way by a small tilt of the low-finesse etalon. In this way, the problem of image distortion by ghosts can be effectively reduced. Therefore, the modification to the simulation code would be adding an offset in the angle distribution Θ. This can be implemented in the code for future purposes.

Also, the pupil apodization, which is introduced in Ref. 16, was partly unattended. We modeled the wavelength shifts and neglected the defocusing effect. In Ref. 11, it is shown that for $f\# \geq 200$ the introduced wavelength shifts $\Delta\lambda$ and the corresponding induced Doppler velocity errors are well below $\Delta v_D < 50$ m/s. Based on demanded VTF measurement accuracy for Doppler velocities and the $f\#$, this effect can be ignored for the VTF.

The simulation is also designed to test the magnetic sensitivity of the instrument. In Ref. 17, it is shown that the polarization due to reflections at each plate surface can be ignored if the angles of incidence are sufficiently small, and the reflectivity coefficients are identical. We limited the maximum angle of incidence to $\varphi_{\max} < 5$ deg. Therefore, instrumentally induced polarization is not modeled. Based on the small angles of incidence, we did not model any losses through outcoupling of the cavities. To derive the impact on polarimetric measurements due to optical elements, the modulation matrix M should be adjusted.

6 Outlook

The developed algorithm enables us to test different instrument configurations and data calibration algorithms. Applying the measured plate error 2-D maps on, e.g., simulated magneto-hydrodynamic (MHD) data cubes of the quiet Sun, gives us the opportunity to clarify the needed surface quality and spectral resolution to meet the required measurement accuracy for remarkable new science with the DKIST. Additionally, it is possible to test a defocused mounting of the etalons in the optical path (see Fig. 6) to study its effect and give meaningful values for the distances d_i to the focal plane. Furthermore, different observational setups can be simulated to define meaningful exposure times t_{exp} and to decide if accumulations n_{ac} are needed to get the requested magnetic sensitivity (preparation for science use cases).

With this algorithm, we have the opportunity to perform end-to-end simulations for solar spectropolarimetric instruments. For future instrument designs, this tool enables the community to define instrumental parameters based on simulated observational errors to verify the demanded measurement accuracy. Therefore, one can test different etalon parameters and setups. Furthermore, by estimating the errors using our algorithm it is now possible to evaluate a designed instrument and calibration algorithms to minimize the instrumental impact. We learned that it is not valid to design an instrument with high spectral resolutions, i.e., $\text{SR} = \frac{\lambda_0}{\delta\lambda} \geq 200,000$ (spectral band width $\delta\lambda = 3.1$ pm) without taking into account the plate quality, photon noise, spatial resolution, and calibration algorithms simultaneously; the transmission of the instrument is strongly distorted by the plate roughness and reflectivity errors. For SR = 200,000, the amount of photons in the detector plane corresponds to photon noise of $\approx 1\%_{\lambda_0=630.25\text{ nm}}$ for $t_{\text{exp}} = 25$ ms. Based on demanded magnetic sensitivity of $B = 20$ G, this requires longer exposure times or accumulations. Accounting for the spatial resolution and typically involved horizontal velocities means there is a well-defined time scale in which the signal detected in one pixel is moved to neighboring pixels. With the developed tool, this can be evaluated and instrument design can be adjusted accordingly. Now, it is possible to make the trade-off between spectral, spatial resolution, and measurement sensitivity for instrument development. For the VTF, we reduced the spectral resolution from SR ≈ 200,000 to SR ≈ 100,000 at $\lambda_0 = 630.25$ nm to achieve the demanded measurement accuracies. Because of the highly customizable code, different spectropolarimetric instruments based on FPIs

also for nonsolar approaches can be simulated and evaluated to study their impacts and test calibration algorithms on simulated observations.

References

1. T. Rimmele et al., "Daniel k. Inouye solar telescope: overview and status," *IAU Gen. Assem.* **22**, 2255176 (2015).
2. T. J. Kentischer et al., "The visible tunable filtergraph for the ATST," *Proc. SPIE* **8446**, 77 (2012).
3. G. B. Scharmer et al., "CRISP spectropolarimetric imaging of penumbral fine structure," *Astrophys. J. Lett.* **689**, L69–L72 (2008).
4. T. J. Kentischer et al., "TESOS, a double Fabry–Pérot instrument for solar spectroscopy," *Astron. Astrophys.* **340**, 569–578 (1998).
5. K. G. Puschmann et al., "The GREGOR Fabry–Pérot interferometer," *Astron. Nachr.* **333**, 880–893 (2012).
6. F. Cavallini, "IBIS: a new post-focus instrument for solar imaging spectroscopy," *Solar Phys.* **236**, 415–439 (2006).
7. M. Born et al., *Principles of Optics: Electromagnetic Theory of Propagation, Interference and Diffraction of Light*, Cambridge University Press, Cambridge, United Kingdom (2000).
8. C. Beck et al., "A polarization model for the German Vacuum Tower Telescope from in situ and laboratory measurements," *Astron. Astrophys.* **443**, 1047–1053 (2005).
9. C. Beck et al., "Polarimetric littrow spectrograph—instrument calibration and first measurements," *Astron. Astrophys.* **437**, 1159–1167 (2005).
10. G. Thuillier et al., "The solar spectral irradiance from 200 to 2400 nm as measured by the SOLSPEC spectrometer from the Atlas and Eureca Missions," *Sol. Phys.* **214**, 1–22 (2003).
11. O. von der Lühe and T. J. Kentischer, "High spatial resolution performance of a triple Fabry-Pérot filtergraph," *Astron. Astrophys. Suppl. Ser.* **146**, 499–506 (2000).
12. A. Tritschler et al., "High-resolution solar spectroscopy with TESOS—upgrade from a double to a triple system," *Sol. Phys.* **211**, 17–29 (2002).
13. M. Matsumoto and T. Nishimura, "Mersenne twister: a 623-dimensionally equidistributed uniform pseudo-random number generator," *ACM Trans. Model. Comput. Simul.* **8**(1), 3–30 (1998).
14. N. Ismail et al., "Fabry–pérot resonator: spectral line shapes, generic and related airy distributions, linewidths, finesses, and performance at low or frequency-dependent reflectivity," *Opt. Express* **24**, 16366 (2016).
15. G. B. Scharmer, "Comments on the optimization of high resolution Fabry-Pérot filtergraphs," *Astron. Astrophys.* **447**, 1111–1120 (2006).
16. J. M. Beckers, "On the effect of narrow-band filters on the diffraction limited resolution of astronomical telescopes," *Astron. Astrophys. Suppl. Ser.* **129**, 191–194 (1998).
17. W. A. Traub, "Polarization effects in stellar interferometers," in *European Southern Observatory Conf. and Workshop Proc.*, Vol. 29, pp. 1029–1038 (1988).

Biographies for the authors are not available.